

## Effect of Mach Number on Secondary Flow Characteristics

Kristina S. Hermanson and Karen A. Thole\*

*Mechanical Engineering Department, University of Wisconsin, USA*

### Abstract

Endwall secondary flows in gas turbines are complicated by highly non-uniform combustor exit profiles. Most experimental endwall studies do match turbine Reynolds numbers, but not Mach numbers, and assume constant temperature conditions with a simple turbulent boundary layer. This paper presents results for benchmarking of a CFD code with experimental data and the effects of inlet profiles at both low and high Mach number conditions under matched Reynolds number conditions. Detailed flowfield measurements were obtained in a large scale, linear turbine vane cascade and were used for CFD benchmarking. Analysis of the results for spanwise varying inlet profiles indicate that the stagnation pressure gradient is the key parameter in determining the character of the secondary flows in the first stator vane passage. Temperature gradients applied at the inlet were distorted in relation to the secondary flows influencing heat transfer to the vane and the inlet thermal field for the next rotor stage. Comparisons of CFD simulations at engine operating Mach number and Reynolds number conditions to the low-speed wind tunnel simulations indicate that the secondary flow pattern develops similarly up to the location of the shock.

### Nomenclature

$C, C_x$  = true and axial chords of stator vane  
 $Ma$  = Mach number  
 $\dot{m}$  = mass flow through passage  
 $n$  = coordinate normal to inviscid streamline  
 $P_o, p$  = total and static pressure  
 $P$  = pitch  
 $Re$  = Reynolds number based on true chord  
 $s$  = coordinate aligned with inviscid streamline, vane surface distance from stagnation  
 $S$  = full span of stator vane  
 $T$  = static temperature  
 $U, V, W$  = absolute velocity components  
 $u, v, w$  = secondary flow plane, transformed velocity components  
 $V$  = velocity magnitude  
 $V_s$  = streamwise velocity,  $u \cos \Psi_{ms} + v \sin \Psi_{ms}$   
 $V_n$  = normal velocity,  $-u \sin \Psi_{ms} + v \cos \Psi_{ms}$

$V_z$  = spanwise velocity,  $w$   
 $X, Y, Z$  = absolute, stationary, coordinate system  
 $x, y, z$  = distances normal, tangent, and spanwise to the secondary flow plane  
 $Y_s$  = pressure loss coefficient,  

$$1/\dot{m} \iint \rho u \left[ \frac{2(p_{o_{inlet}} - p_o)}{\rho U_{inlet}^2} \right] dA$$
  
 $z^+$  = inner coordinates spanwise distance,  
 $z(\tau_w/\rho)^{0.5} / \nu$

### Greek

$\delta, \delta^*, \theta$  = boundary layer, displacement, and momentum thicknesses  
 $\varepsilon$  = turbulent dissipation  
 $\Phi_s$  = normalized pitchwise pressure gradient,  

$$\frac{\partial p_s}{\partial P} \frac{C}{\rho V^2}$$
  
 $\nu$  = kinematic viscosity  
 $\rho$  = density

\*To whom correspondence should be addressed at:  
 Mechanical Engineering Department  
 Virginia Polytechnic Institute and State University  
 Blacksburg, VA 24061-0238, USA  
 Phone: (540)231-7192/FAX: (540)231-9100  
 E-mail: thole@vt.edu

$\Omega_z$  = streamwise vorticity,  $\Omega_x \cos(\Omega_{ms}) + \Omega_y \sin(\Omega_{ms})$

$\Omega_x$  = x-vorticity,  $\frac{\partial W}{\partial Y} - \frac{\partial V}{\partial Z}$

$\Omega_y$  = y-vorticity,  $\frac{\partial U}{\partial Z} - \frac{\partial W}{\partial X}$

$\tau_w$  = wall shear stress

$\psi_{ms}$  = midspan yaw angle,  $\tan^{-1}(v_{ms}/u_{ms})$

#### Subscripts

*ave* = average

*ex* = exit

*inlet* = inlet value at mid-span

*ms* = mid-span values

#### Introduction

Turbine durability in the endwall region of the first stage stator vane is critical as hotter combustion products are necessary to increase the power generated in the gas turbine. The hot gas combined with the motion of endwall secondary flows creates a harsh environment for the turbine platform. The complexity of the secondary flow field is worsened when considering both the spanwise and pitchwise variations in velocity, temperature, and pressure that exit the combustor and approach the first stage vane. Cooling jets swirled inside the combustor result in inlet profiles to the vane that are highly non-uniform and difficult to model in wind tunnel experiments.

Endwall flowfield studies are typically modeled in a scaled-up low-speed wind tunnel cascade. The low-speed conditions match the vane or rotor Reynolds number, but not the Mach number resulting in a different loading on the vane. Shocks occurring at high speed conditions are also not accurately modeled in the low-speed scaling. It is useful to assess how the secondary flow development compares between low and high Mach number conditions.

Results from a previous study (Hermanson and Thole, 2000) for a low-speed parametric study that considered effects of different combinations of velocity and/or temperature (density) inlet profiles on resulting secondary flows are briefly summarized in this paper. The CFD simulations were performed

for a commercial turbine vane geometry at matched Reynolds number conditions to allow direct comparison with measured velocities in a large-scale wind tunnel simulation. This paper presents a similar analysis comparing and contrasting high and low Mach number conditions. Prior to that discussion, the past literature, computational methodology, and additional code benchmarking is presented.

#### Relevant Past Studies

To relate high regions of endwall heat transfer to secondary flow patterns and to provide a visual representation of flow through the turbine passage, a number of flow models have been proposed. The flow model for a vane, presented by Langston (1980), shows two legs of the horseshoe vortex are formed. The pitchwise pressure gradient generated across the blades prompts the pressure side leg to merge with and become part of the passage vortex. The suction side leg remains in the corner near the endwall and suction surface and exits the blade row as a counter rotating vortex inside the passage vortex, later referred to as a corner vortex. Langston (1980) noted that the corner vortex may be dissipated due to viscous effects. The model proposed by Sharma & Butler (1987) indicated a suction side horseshoe vortex that begins to lift off the endwall and actually orbit about the passage vortex at the location of the minimum pressure point in the passage.

Highly distorted radial and circumferential temperature distributions at the combustor exit have been previously given by Suo (1985), Halls (1970), and Crocker *et al.* (1998). The predictions from Crocker *et al.* (1998) showed highly distorted velocity and pressure profiles that are not represented by assuming a turbulent inlet boundary layer for the endwall. Pitchwise and spanwise temperature profiles were investigated by Boyle and Giel (1997) using a parabolic radial temperature profile with the highest temperature occurring at the midspan. The results of Boyle and Giel (1997) were consistent with the work of Butler *et al.* (1989) in that no significant difference in flow through the stator was observed due to a temperature distortion.

However, in both cases there was a segregation of hot and cold fluid in the rotor with the higher temperatures on the pressure side. This trend was also noted in an unsteady analysis of flow in a turbine stage by Dorney *et al.* (1992). Stabe *et al.* (1984) performed experiments with an axisymmetric radial inlet temperature profile. Little effect of the profile on the turbine was noted; however, the temperature profile tested had a ratio of maximum to minimum temperature of only 1.2 compared to a factor of up to 2.0 which can reportedly be measured in a gas turbine (Butler *et al.*, 1989).

There have been a few experimental studies on the effect of Mach number on secondary flows in a turbine cascade which include Sieverding and Wilputte (1981) and Perdichizzi (1990). Flowfield data reported by these two studies were only downstream of the airfoil trailing edge and indicated that the Mach number does affect secondary flow and loss. As the Mach number increased, the flow in the endwall region more closely followed the turning angles at the midspan. Koiro and Lakshminarayana (1996), validated a CFD code with the results of Perdichizzi (1990) and further concluded that a thinner endwall boundary layer associated with higher Mach numbers reduced the endwall cross flow downstream of the airfoil trailing edge. These studies point out that there is a Mach number effect on the flow downstream of the trailing edge. It is important to recognize, however, that downstream of the airfoil a trailing edge vortex is generated in addition to both the passage vortex and remnants from the leading edge suction side vortex. It is quite likely that this trailing edge vortex is affected by the Mach number.

## Experimental Design

A flowfield measurement plane near the vane leading edge and six additional planes (Kang and Thole, 2000) were obtained from a scaled-up turbine vane experiment in a low speed wind tunnel shown in Figure 1. Note that in the comparison with experimental data, planes orthogonal to the turbine vane are evaluated in the comparison with experimental data, and axial planes are evaluated in

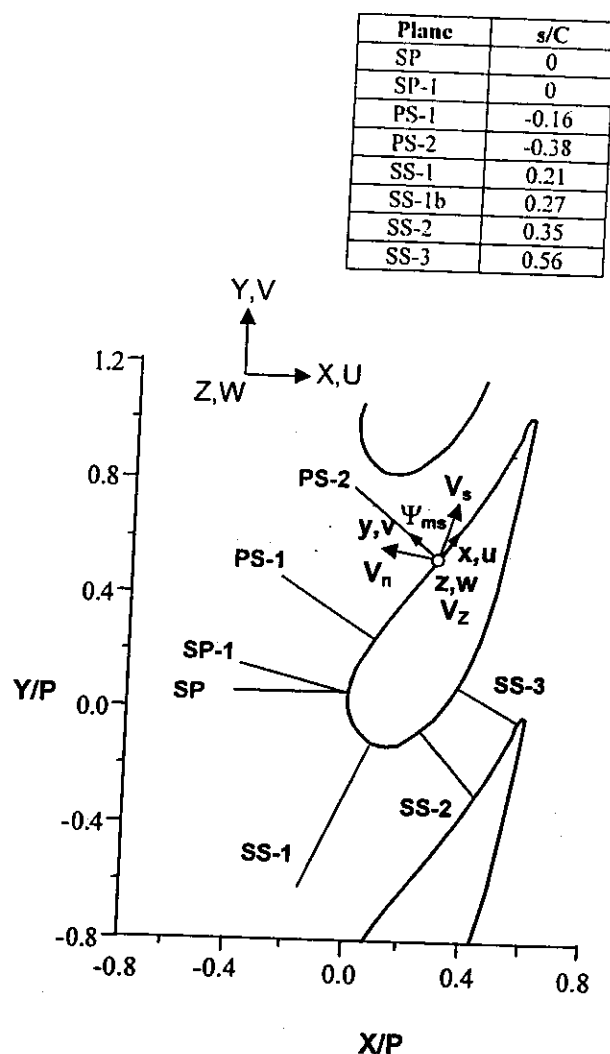


Fig. 1: Locations and coordinates of seven planes used for benchmarking CFD with experimental measurements and secondary flow analyses.

the comparison between high and low Mach number cases. The vane considered in this study was scaled up by a factor of nine in the experiments to achieve detailed flowfield measurements of the endwall secondary flows. Characteristics of the turbine vane geometry and inlet flow conditions for the comparison between the CFD predictions and experiments are summarized in Table 1. The experimental test conditions in this study are equivalent to those described by Kang *et al.* (1999).

The corner test section of the wind tunnel, where

**Table 1**  
Stator Vane Geometry and Inlet Flow Characteristics

Actual chord length	6.60 cm
Scaling factor	9
Scaled-up chord length	59.4 cm
Pitch/chord	0.77
Span/chord	0.93
Axial chord/chord	0.48
Exit Reynolds number	$1.2 \times 10^6$
Flow inlet angle	$0^\circ$
Flow exit angle	$78^\circ$
$\delta_{99}/S$	0.091
$\delta^+ / S$	0.019
$\theta/S$	0.129

the vane was installed, is shown in Figure 2. Endwall splitter plates were installed  $4.6C$  upstream of the stator vane stagnation to control the boundary layer growth on the top and bottom endwalls. Trip wires placed  $3.9C$  upstream of the vane cascade were used to ensure a fully turbulent boundary layer. Side wall boundary layers were also removed using two streamwise suction slots at the inner and outer

leading edges. The test section consists of one central vane as well as two adjacent leading edges to ensure periodicity and proper modeling of the passage vortex. The outer leading edge is attached to a flexible wall that is adjusted to match the geometry of the adjacent vane. Downstream of where the adjacent vane ends, the wall is positioned to match the pressure distribution from a two-dimensional

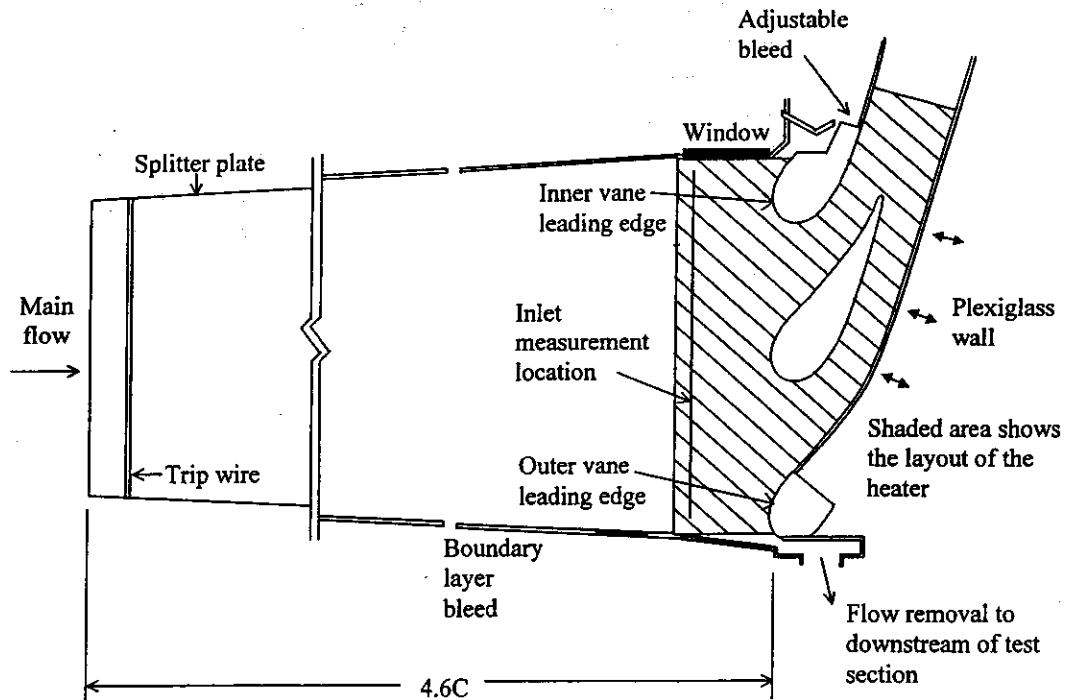


**Fig. 2:** Top view of corner test section.

inviscid periodic CFD prediction.

All three components of velocity, both tangent and normal to each measurement plane, were measured using a back-scatter fiber optic LDV system as described by Kang *et al.* (1999). Uncertainties were based on a 95% confidence interval using the method described by Moffat *et al.* (1988). The uncertainties of  $V_u$ ,  $V_n$ , and  $V_z$  are 1%, 7.5%, and 1.5% respectively. These uncertainties represent the worst possible case being calculated near the vane-endwall surfaces.

### Computational Methodology

All of the computations presented in this report were performed with a commercial software package by Fluent Inc (Fluent, 1998). The package offers solution adaptive grid capabilities used with pressure-based flow solvers for incompressible and compressible flows. Two different variations of the Fluent code were used in the CFD simulations including RAMPANT for compressible flow and FLUENT/UNS for incompressible flow. Second order discretization was used for energy, and turbulence, and the Reynolds Averaged Navier Stokes (RANS) equations. FLUENT/UNS is a segregated solver with the pressure and velocity coupled using the Semi-Implicit Method for Pressure-Linked Equations (SIMPLE) algorithm (Patankar, 1980). RAMPANT solves the conservation equations for continuity, momentum, and energy simultaneously using an explicit, multi-stage, time-marching scheme.

The computational domain for the low speed and high speed simulations is depicted in Figure 3. The domains in Figure 3 consist of approximately 800,000 unstructured cells before adaptations (additional adaptations were performed for the high speed case to resolve the shock occurring on the suction surface). The inlet boundary condition is placed 75% of a chord length ( $0.75C$ ) upstream of the blade stagnation and the outlet boundary condition is placed  $1.5C$  downstream along a line directed with the exit flow angle of the vane for all domains. For both the low and high speed conditions

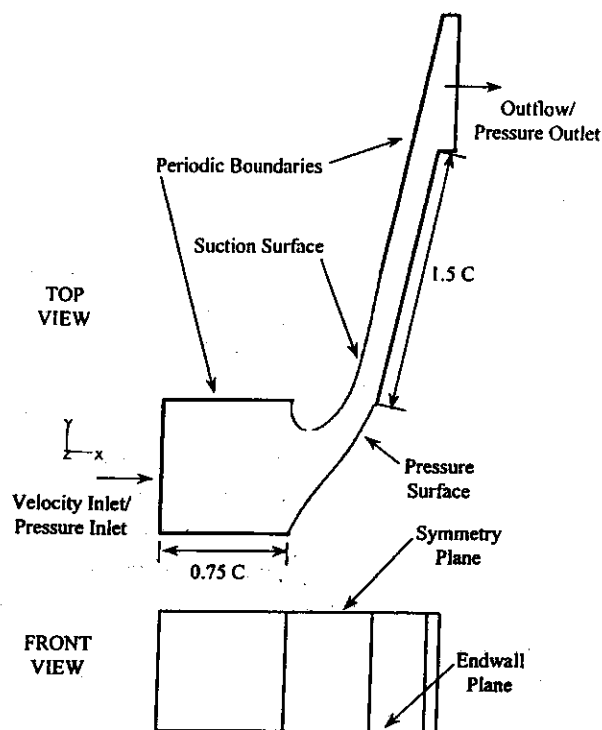


Fig. 3: Computational domain for CFD simulations.

the placement of the inlet and outlet boundary conditions were determined by two-dimensional CFD analyses insuring that the flow was not affected by the vane at these locations. Periodic boundary conditions are placed between the inlet, blade surface, and outlet with the vane being split across the pitch at the location of the dynamic stagnation point.

The inlet boundary condition on the endwall surface was obtained using a two-dimensional boundary layer code TEXSTAN (Crawford, 1986). The major difference in the domain for the low and high speed calculations is in the boundary conditions used at the inlet and outlet. For the low speed cases a velocity inlet was used with a specified velocity, static temperature, turbulent kinetic energy ( $k$ ) and turbulent dissipation ( $\epsilon$ ). At the outlet an outflow condition with a zero normal gradient for all variables except pressure is assumed. For the high speed cases a pressure inlet was used with a specified total pressure, total temperature,  $k$ , and  $\epsilon$ .

At the outlet a constant static pressure was specified. The static pressure for both the low speed and high speed cases were approximately constant at the inlet for all simulations. The entire domain of each numerical simulation was initialized to the values prescribed at the inlet.

Prior to performing the simulations, grid insensitivity was verified through a study using three different mesh sizes (Hermanson and Thole, 2000). As a check on the grid sensitivity, the mass averaged total pressure losses at several different positions through the cascade passage were calculated. Figure 4 compares the total pressure loss coefficients for all three mesh sizes. The results of Figure 4 indicate that there are no differences between the two largest mesh sizes and an underprediction for the smallest mesh size. For these studies the  $8 \times 10^5$  cell mesh size was considered to be grid-insensitive.

Numerical uncertainty due to grid sizes and convergence was determined by comparing the change in lift force on the pressure and suction surface relative to the baseline case. Lift force is defined as the  $Y$ -component of force ( $Y$ , as defined in Figure 1) on the pressure and suction surfaces obtained by integrating the static pressure over the vane. Results were compared with the

solution-adapted mesh ( $1.3 \times 10^6$  cells) resulting in a 1.3% difference as compared with the  $8 \times 10^5$  cell mesh. The baseline conditions computed on the  $8 \times 10^5$  cell mesh were also simulated for an additional 100 iterations to judge the convergence uncertainty resulting in a 0.23% difference in the lift force prediction. The results of percent difference in variables between the high Mach number baseline and a solution with 200 more iterations was 0.10%.

Prior to performing the low-speed parametric study, the standard  $k-\epsilon$  (Lauder and Spalding, 1974) and RNG  $k-\epsilon$  (Yakhot *et al.*, 1992) turbulence models were compared based on their ability to model the horseshoe vortex roll-up on Plane SP. Note that the node spacing near the endwall for the CFD was set to achieve  $30 < z^+ < 60$  in the passage to insure proper usage of the wall functions. Based on the comparison of the predictions with the measurements presented by Kang *et al.* (1999), the RNG  $k-\epsilon$  model better predicted the horseshoe vortex location and roll-up and thus was used in this study.

To compare secondary flowfields between cases with different inlet conditions the flowfield was plotted at different locations around the vane to visualize the passage vortex. The vectors which

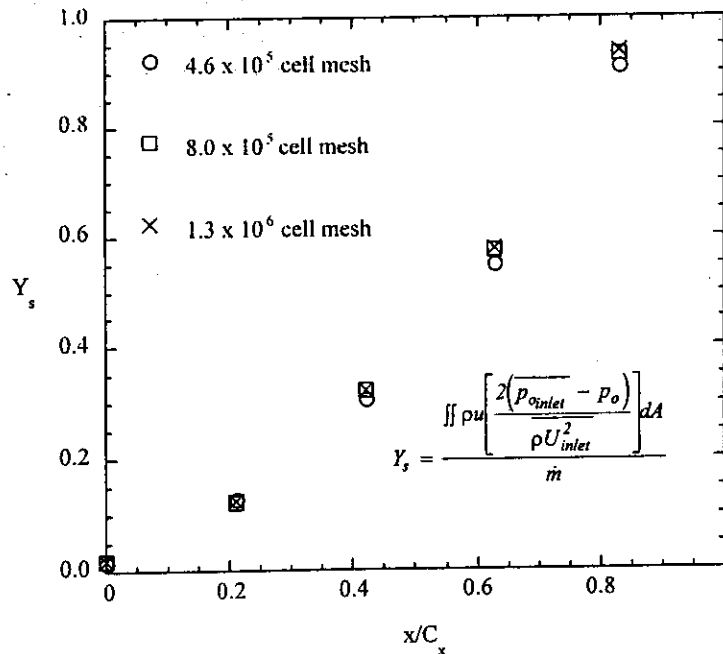


Fig. 4: Mass averaged total pressure loss,  $Y_s$ , for three mesh sizes.

graphically represent the passage vortex were determined by transforming the local velocities ( $u$ ,  $v$ ,  $w$  or  $U$ ,  $V$ ,  $W$  in Figure 1) into the mean flow direction ( $V_s$ ,  $V_m$ , and  $V_z$ ) based on the midspan flow turning angle ( $\Psi_{ms}$ ) using the relations defined in the nomenclature. The secondary flow vectors are plotted using the components normal to the mean flow direction ( $V_m$ ,  $V_z$ ) with the observation direction looking downstream for planes on both the suction and pressure surfaces.

### Test Matrix Description

By applying a combination of inlet conditions to the successfully benchmarked computational domain, the effects of velocity, temperature, pressure, and Mach Number could be analyzed. A summary of these inlet conditions is given in Table 2. The inlet profiles and detailed results from the low Mach number cases were previously documented by Hermanson and Thole (2000) and will briefly be described in this paper. For all of the computed cases the static pressure is constant at the inlet, and the static temperature is specified. The first case shown in Table 2 describes what will be referred to as the baseline case and is directly comparable with the experimental measurements.

The total temperature profiles used in Cases 2, 3,

4a, and 4b are linear from 0 - 32% span and are based on engine data (Kvasnak, 1997). This temperature gradient is also similar to the profile of Boyle and Giel (1997). For the constant Mach number case the mass averaged static temperature is equal to the uniform temperature of the baseline. For the cases of the constant velocity and constant inlet Mach number (Cases 3, 4a, and 4b) there is only a thin boundary layer that forms as the flow approaches the vanes. For the constant inlet Mach number cases, the velocity profiles were calculated using the definition of the Mach number and the specified static temperature profiles.

After completion of the parametric study, the baseline case (Case 1a) and the constant inlet Mach number of Case 4a were also chosen to simulate at engine high Mach number conditions to verify the theory proposed from the low-speed analysis. For the high Mach number CFD cases, the total pressure profile was calculated using compressible flow relations and the boundary layer velocity profile. The calculation is based on using the midspan stagnation pressure and static temperature for engine operating conditions (Johnson, 1996). At the pressure outlet a constant static pressure was set that is equal to the static pressure at the vane tip based on a previously given high Mach number 2-D inviscid simulation (Johnson, 1996).

Table 2  
Summary of Baseline and CFD Test Matrix,  $Re_m = 2.4 \times 10^5$

Case Number	Velocity Profile Characteristics	Inlet/Exit Mach Number	$T_{wall}/T_{max}$	$T_{wall}/T_{ave}$
1a (Baseline)	$\delta/S = 9.1\%$	0.012 / 0.09	1	1
1b	$\delta/S = 9.1\%$	0.12 / 0.85	1	1
2	$\delta/S = 9.1\%$	0.012 / 0.09	0.63	0.73
3	$U = \text{Constant}$	0.012 / 0.09	0.63	0.73
4a	$\text{Mach} = \text{Constant}$	0.012 / 0.09	0.63	0.73
4b	$\text{Mach} = \text{Constant}$	0.12 / 0.85	0.89	0.92

### Comparison of Computations and Experiments at Low Mach Number Conditions

The untransformed velocity vectors ( $u$ ,  $w$ ) in Plane SP-1, a plane that intersects the vane stagnation location and is orthogonal to the vane, is shown in Figure 5a and 5b for both measurements and predictions. Note that the data from the

unstructured mesh is interpolated onto a uniform grid to avoid concentration of data points near the endwall and to improve overall visualization. There is a good agreement between the plots, with the center of the vortex for the predictions being slightly further from the vane stagnation.

The transformed secondary flowfield vectors ( $V_m$ ,  $V_z$ ) with contours of streamwise velocity ( $V_x/U_{inlet}$ ) are plotted in Figure 6a and 6b for Plane

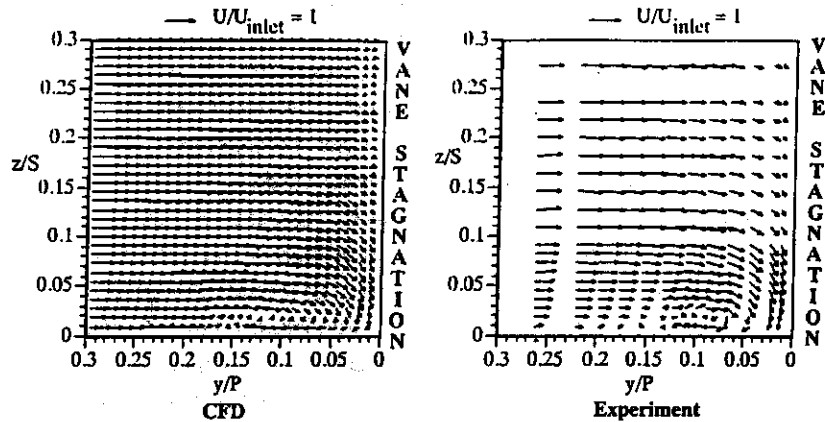


Fig. 5a-b: Flowfield on Plane SP-1 ( $u, w$  components of velocity) for CFD simulation and experiment.

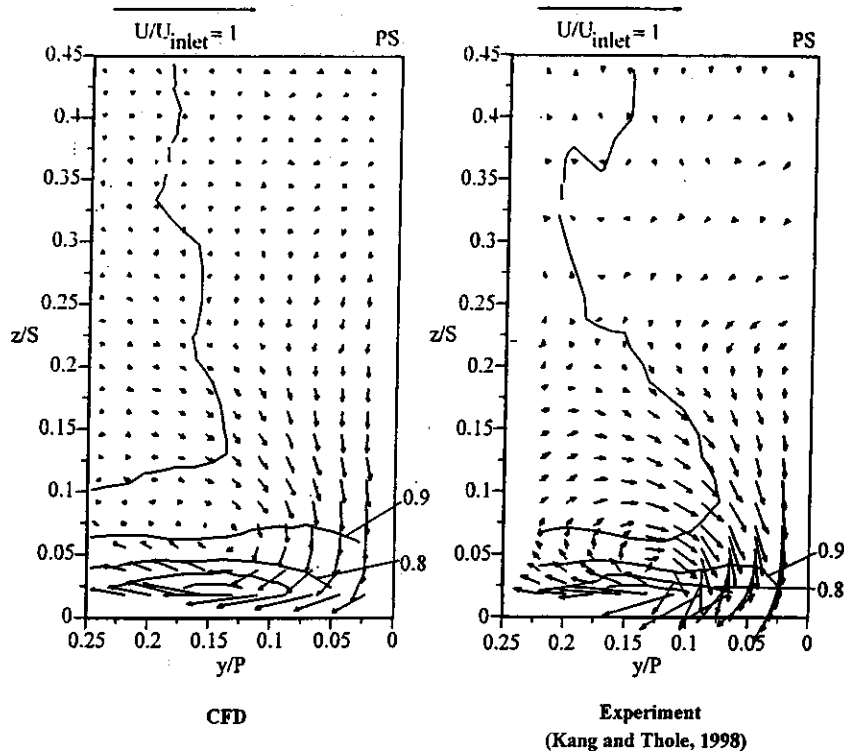
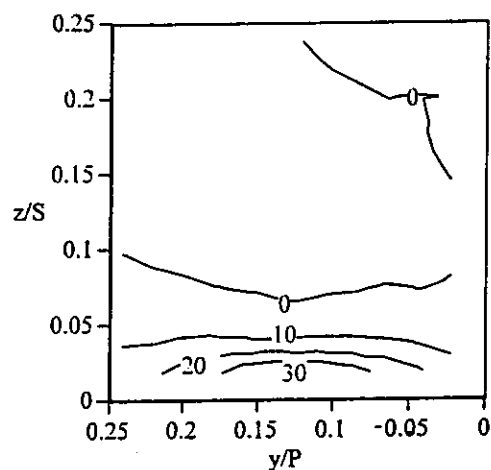


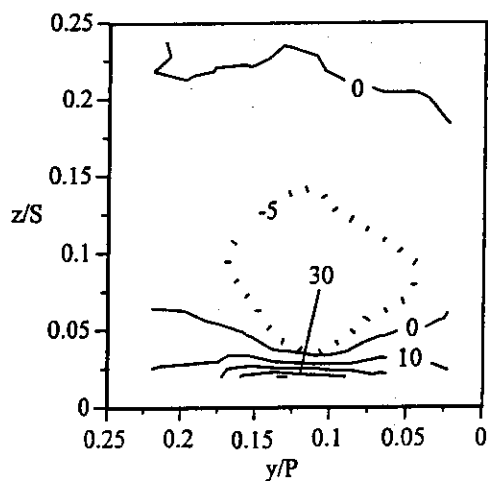
Fig. 6a-b: Secondary flowfield and streamwise velocity,  $V_x/U_{inlet}$ , comparison between CFD and experiment on Plane PS-1.



PS-1 located at  $s/C = -0.16$ . Again there is good agreement on this measurement plane. The vortex center is predicted at  $y/P = 0.13$ ,  $z/S = 0.05$  and for the measurements it is at  $y/P = 0.12$ ,  $z/S = 0.03$ . The prediction of the vortex being slightly further off the endwall than measured is consistent for most downstream measurement planes. The shape of the secondary flowfield looks similar to the experimental data with the CFD showing slightly higher magnitudes of flow moving towards the pressure surface in the vortex. A good agreement is also seen between the yaw angles on Plane PS-1, shown in Figure 7a and 7b. These angles represent



a) CFD

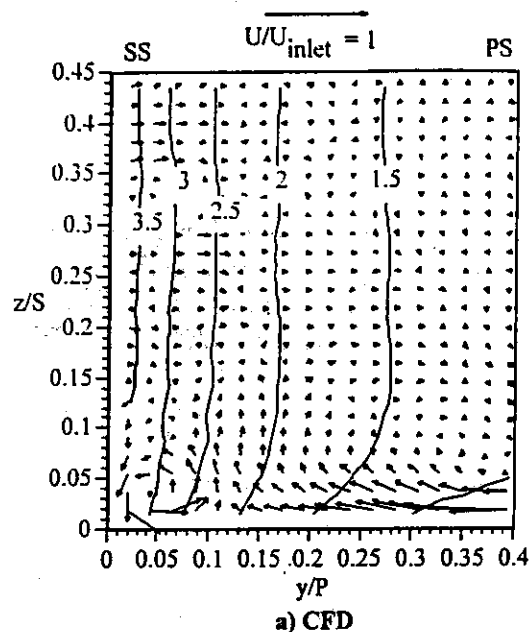


b) Experiment

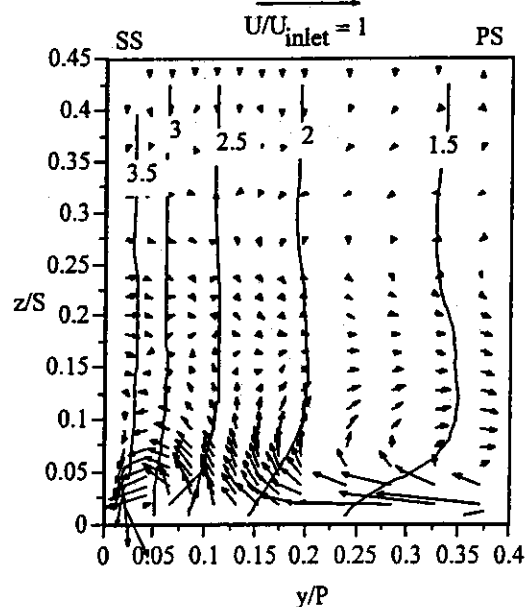
Fig. 7a-b: Yaw angles ( $\psi - \psi_{ms}$ ) on Plane PS-1.

the deviation of the flow near the endwall from the flow occurring near the vane midspan.

The secondary flowfield and streamwise velocity for Plane SS-1 is presented in Figure 8a and 8b. The suction side leg of the horseshoe vortex is present at  $y/P = 0.04$ ,  $z/S = 0.03$  for CFD and  $y/P = 0.05$ ,  $z/S =$



a) CFD



b) Experiment

(Kang and Thole, 1998)

Fig. 8a-b: Flowfield and streamwise velocity,  $V_s/U_{inlet}$ , on Plane S-1.

0.03 for the experiment. The passage vortex is also present out to  $y/P = 0.4$ . The passage vortex shows more skewing of the streamwise velocity in the experimental data very near the wall than the CFD. Comparison between CFD and experiment on Plane PS-2, SS-2, and SS-3 also showed good agreement between the predicted and measured secondary flow development.

### Effect of Inlet Profiles for Low Mach Number Conditions

The CFD prediction of the flow pattern for the low speed, matched Reynolds number simulations (Case 1a) is presented in Figure 9. This flow pattern was created by tracing the pathlines of particles released at 0-13% span at  $x/C = -0.17$  upstream of the vane stagnation from  $0.9 < y/P < 1$ . The baseline case results in a flow model similar to that proposed by Langston (1980). The horseshoe vortex develops

at the leading edge with a pressure side and suction side leg. Flow from high in the boundary layer and above the boundary layer forms the passage vortex on the pressure side or joins the suction side leg of the horseshoe vortex. Flowfield analysis of cases with a spanwise temperature gradient showed that the magnitude of secondary flows and streamwise vorticity were reduced when a temperature gradient was applied simultaneously with a turbulent inlet boundary layer. When a temperature gradient was applied with a constant inlet velocity a large vortex was formed with the opposite rotation direction as the baseline case, as discussed by Lakshminarayana (1975). This vortex had little streamwise vorticity and occupied most of the passage. For the case of a constant inlet Mach number and total pressure, Cases 4a, no vortex structures were formed; however, there was a cross-flow velocity component near the endwall due to a developing boundary layer.

These flowfield results were interpreted by using an approximation of streamwise vorticity in the

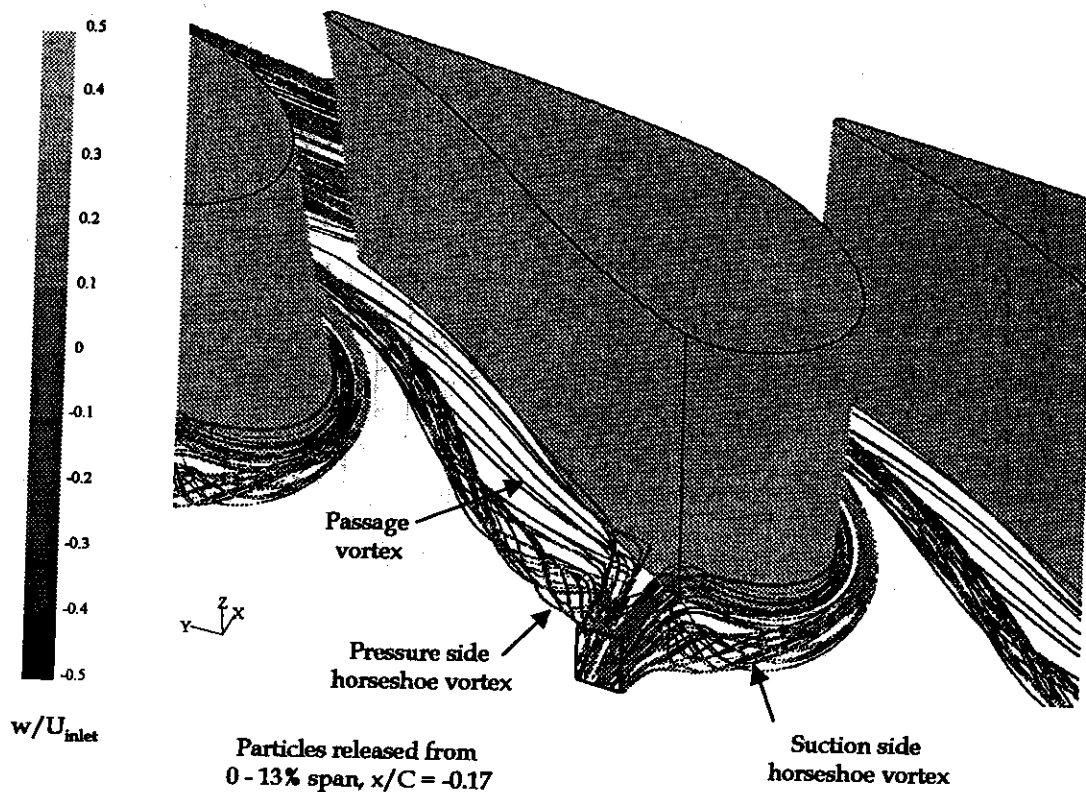


Fig. 9: Particle pathlines for Case 1a,  $\delta/S = 0.091$ ,  $T_{\text{wall}}, T_{\text{max}} = 1$ .

leading edge region given below

$$\Omega_s = \frac{1}{U_\rho} \frac{\partial p_o}{\partial z} \sin \psi_{ms} \quad (1)$$

The approximation is based on the assumptions that the flow is incompressible at the inlet (which occurs even at engine operating conditions) and the gradients in the  $V$  and  $W$  components of velocity are small relative to the velocity gradients in the boundary layer. Since the streamlines are curved near the vane stagnation (up to  $\sim 25^\circ$ ) and spanwise gradients in total pressure are present due to the approaching boundary layer, streamwise vorticity develops in the form of a horseshoe vortex. For Case 4a there are no gradients in total pressure and therefore no streamwise vorticity is present at the leading edge. This is demonstrated in Figure 10 with particle pathlines released at the same location described in Figure 9. This theoretical comparison is consistent with the theory for an intrinsic coordinate system as discussed by Lakshminarayana (1975). A generalized expression for secondary vorticity

indicated that gradients in total pressure will only generate secondary vorticity when there are accompanying spanwise gradients of entropy or Mach number (or total pressure when the static pressure is assumed constant).

### Effect of Inlet Profiles for High Mach Number Conditions

To determine the effect of Mach number on the secondary flows, two cases were simulated at a Mach number and Reynolds number that matches the engine conditions. These results were used to verify predictions for endwall secondary flows from the low-speed CFD simulations, as well as low-speed wind tunnel experiments.

Figure 11 presents the non-dimensional static pressure,  $C_p$ , for low and high speed simulations (Cases 1a and 1b) at the vane mid-span. The  $C_p$  for the three-dimensional viscous CFD simulation at engine conditions is also compared to the

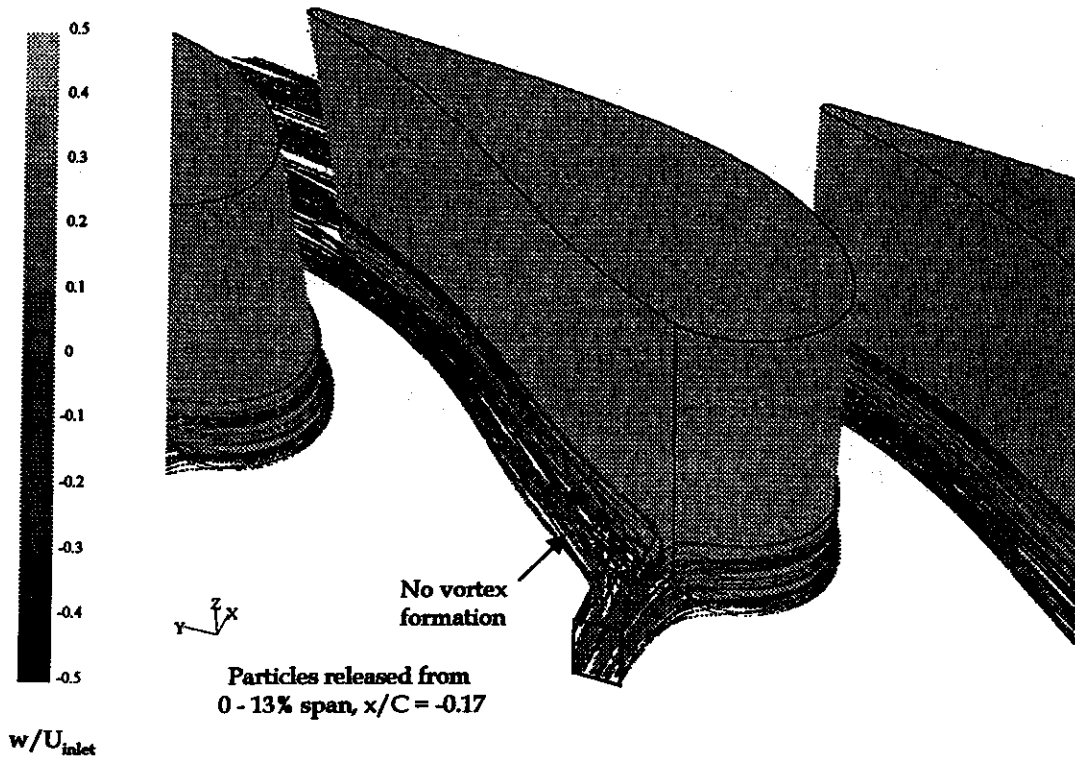


Fig. 10: Particle pathlines for constant inlet Mach number, Case 4a.

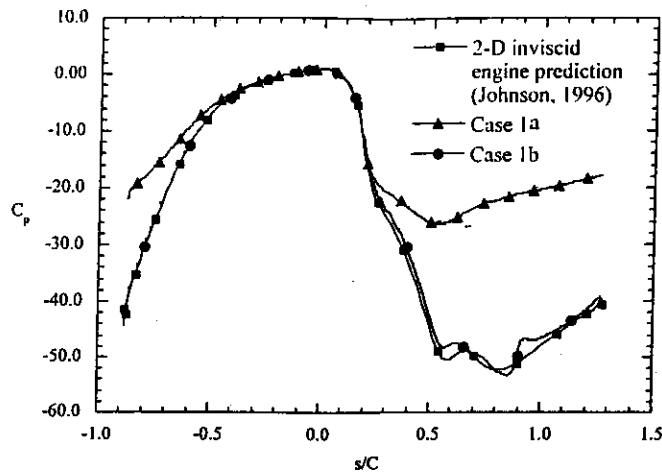


Fig. 11: Static pressure distributions for low and high Mach number CFD simulations.

independent predictions with another CFD code from a two-dimensional inviscid high speed analysis (Johnson, 1996). For both high speed simulations, the  $C_p$  values on the pressure surface has an excellent match. The shock that occurs on the suction surface creates slight discrepancies between the two-dimensional inviscid and three-dimensional viscous distribution. Even after grid-adaptions on static pressure gradients, the shock is predicted at the correct location, but with a slightly larger pressure drop. Comparison of the low and high Mach number pressure distributions yield several possible points that could produce differences in the secondary flow field. In the incompressible region of the flow for engine conditions, from  $\sim -0.3 < s/C < 0.2$ , the non-dimensional pressure distribution is exactly

matched. Beyond this location on both the pressure and suction surfaces flow accelerates more rapidly and there is a much larger pressure drop at engine conditions. The largest differences in the pressure distribution are seen on the suction side because of the shock that occurs. An aft-loaded condition occurs for the high speed case and a fore-loaded condition for the low speed case.

Before comparing the complex flow near the endwall, the freestream mid-span flow surrounding the vane passage was first examined. The midspan flow turning angle at several locations along the axial direction inside the passage and at a location downstream of the trailing edge for the low and high Mach number baselines is presented in Figure 12. The plots for the high and low speed cases are nearly

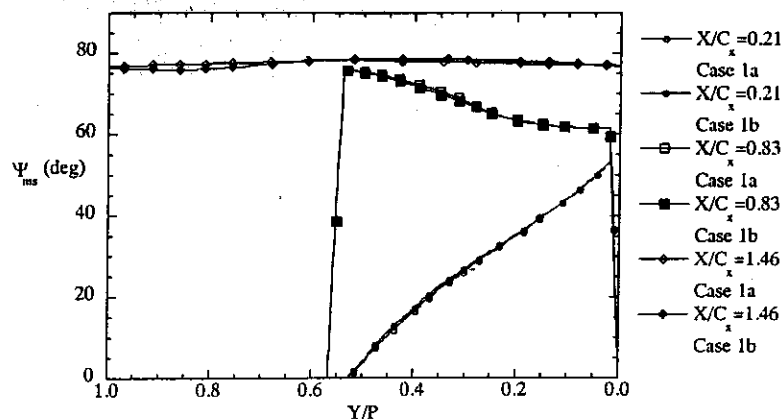


Fig. 12: Midspan flow turning angle,  $\psi_{ms}$ , at several axial locations for low and high Mach number conditions.

identical inside the passage with the low speed having a slightly higher turning angle near the pressure surface at  $X/C_x = 0.21$  and the high speed with a slightly higher turning angle at  $X/C_x = 0.83$ . Even though the midspan velocity distribution shows significant variance between the simulations across the pitch, the midspan streamlines continue to follow the same path, at least within the boundaries of the vane passage. This indicates that the turning is highly a function of the vane geometry. Also, since the secondary flow and streamwise vorticity is calculated using this angle, similarities should be present between the secondary flows of both cases. Downstream of the passage at  $X/C_x = 1.46$  there is a more notable difference in midspan flow angles between the low and high Mach numbers.

The pitchwise averaged flow deviation,  $-\Psi_{ms}$ , from midspan to endwall for the locations within the vane passage and downstream of the trailing edge are shown for Case 1 and Case 1b in Figure 13. The similarity between the low and high Mach numbers inside the passage is clearly demonstrated. At  $X/C_x = 0.21$  and  $X/C_x = 0.83$  the flow deviation is very small from the midspan to  $Z/S = 0.10$  where the pitchwise averaging reveals the cross flow associated with the passage vortex. Downstream of the passage at  $X/C_x = 1.46$ , however,

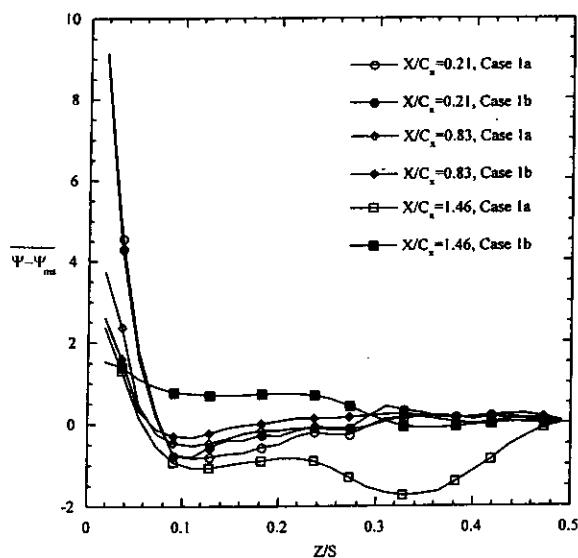


Fig. 13: Pitchwise averaged flow deviation for low and high Mach number simulations.

there is much more underturning and overturning near the endwall for the low speed simulation compared with the high speed simulation. At this location, which is outside of the passage, the low Mach number shows more than twice the magnitude of flow deviation. This result is in agreement with the experimental results of both Sieverding and Wilputte (1981), Perdichizzi (1990), and the computational results of Koiro and Lakshminarayana (1996). In these analyses (which were focused only downstream of the trailing edge), it was concluded that after reaching the choked condition the relative magnitude of primary and secondary velocities reduces the flow deviation. Since three-dimensional flowfield measurements are difficult to make inside the passage at high speed conditions, it is beneficial to use the CFD predictions to determine the effect of Mach number on the flowfield inside the passage.

Figure 14a-b depicts secondary flow vectors and streamwise vorticity at  $X/C_x = 0.21$  for the low and high Mach number cases for the baseline. At this location, although the Mach number is ten times higher, the flow is incompressible for both cases. The plane reveals both the passage vortex and suction side leg of the horseshoe vortex with the flow for each simulation being very similar. The centers of the vortices appear to be at the same location, and a strong spanwise component of velocity is seen at the pressure side up to about 30% span for each case. The streamwise vorticity contours show that there is just slightly more vorticity associated with the vortices of the high speed case and the peak vorticity in the passage vortex occurs slightly further from the pressure surface. The high speed calculations show additional vorticity along the suction surface which may be due to higher levels occurring in the vane boundary layer under high Mach number conditions.

A similar plot for  $X/C_x = 0.83$ , near the end of the passage, is shown in Figure 15a-b. At this location there are large discrepancies in the pressure distribution along the vane due to the flow compressibility. Once again, the secondary flow pattern is very similar between cases. The location of the passage vortex and streamwise vorticity associated with it follow the same trends as pointed

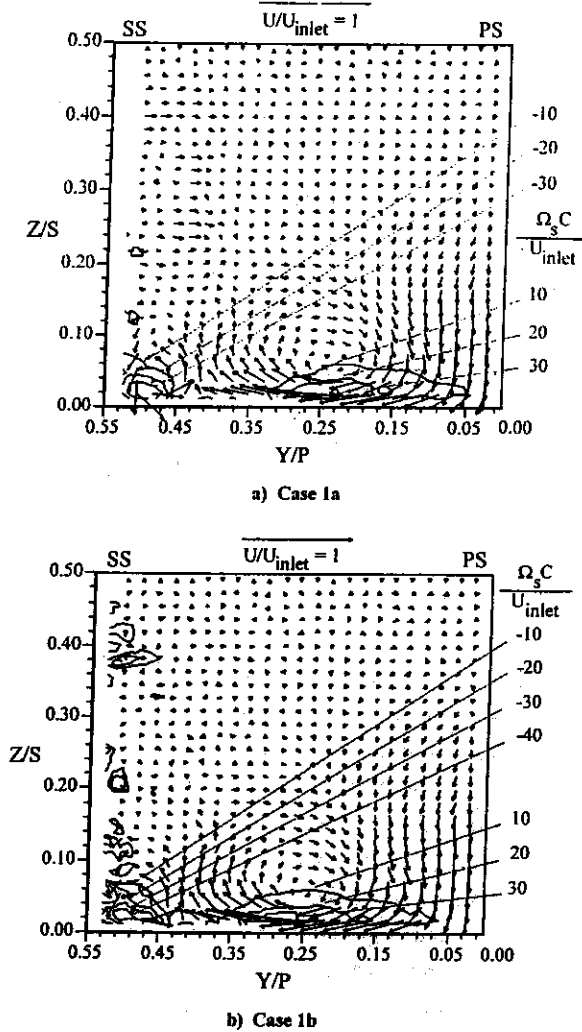


Fig. 14a-b: Secondary flowfield and streamwise vorticity at  $X/C_x = 0.21$  for the baseline case at low speed conditions, Case 1a, and high speed conditions, Case 1b.

out in Figure 14a-b. The high speed case has just slightly higher vorticity levels and the center is a fraction of a pitch further from the pressure surface. The spanwise location of the vortex is in agreement between plots. At  $X/C_x = 0.83$  the suction side leg of the horseshoe vortex has been dissipated by interaction with the passage vortex, and flow is seen to move up along the suction surface. A more notable difference in this plot is that the high speed simulation predicts a significant amount of flow towards the suction surface from the endwall to  $z/S =$

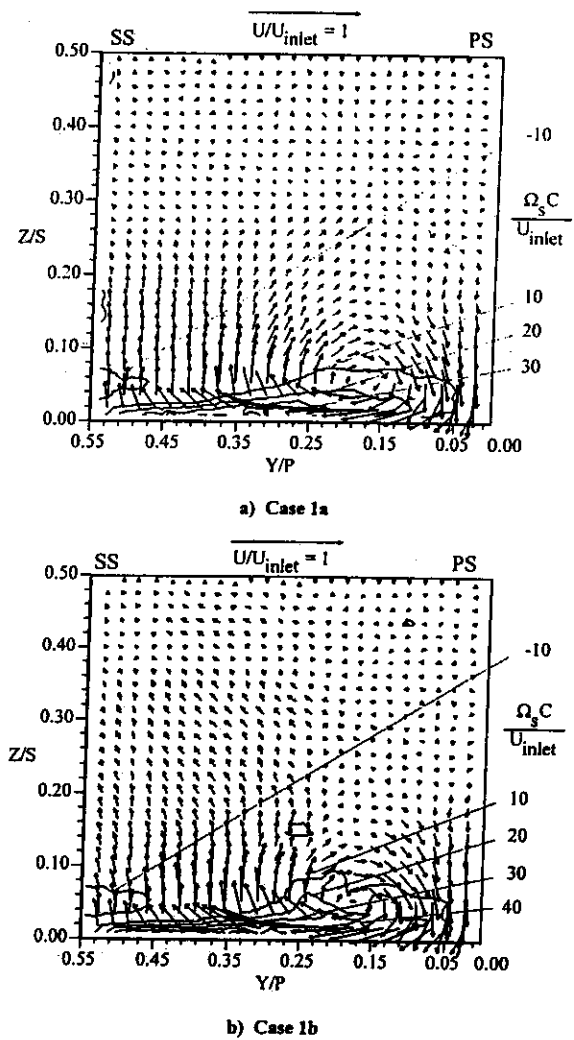


Fig. 15a-b: Secondary flowfield and streamwise vorticity at  $X/C_x = 0.83$  for the baseline case at low speed conditions, Case 1a, and high speed conditions, Case 1b.

0.35. This flow pattern occurs due to the discontinuity associated with the pressure drop across the shock. This plane intersects the suction surface at  $s/C = 0.79$  which is exactly in the low pressure region of the shock (see Figure 11).

The flowfield at  $X/C_x = 0.83$  for Case 4a and Case 4b is shown in Figure 167a-b. The same trends as previously pointed out in the comparison of the baseline cases also occur in these plots. The effect of the shock directing flow towards the suction surface from 15 - 40% span is again present. In this case

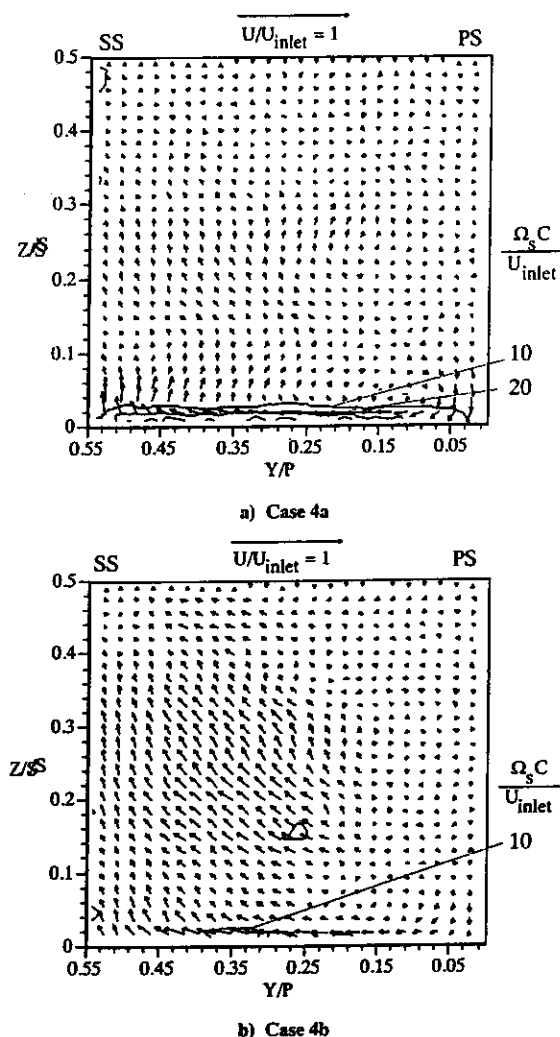


Fig. 16a-b: Secondary flowfield and streamwise vorticity at  $X/C_x = 0.21$  for the constant inlet Mach number case at low speed conditions, Case 4a, and high speed conditions, Case 4b.

there are higher levels of streamwise vorticity for the low speed case near the endwall and more crossflow than the high speed conditions. Since no vortices formed at the leading edge, a boundary layer developed along the endwall through the passage and the spanwise total pressure gradients associated with it yield the streamwise vorticity very near the endwall. The smaller amount of cross flow and streamwise vorticity for the high speed case indicates a smaller boundary layer. The high

momentum of the fluid in the streamwise direction at the engine operating conditions retards the secondary flow motion in the absence of a true vortex structure. The boundary layer may also be affected by the shock at this location. This is consistent with the results of Koiro and Lakshminarayana (1996).

The detrimental effect of the shock is illustrated by plotting total pressure loss along the vane passage for both baseline cases, Figure 17. Here the loss is initially equal since the same inlet boundary layer is used. The total pressure loss is only slightly larger for the engine case until  $X/C_x = 0.83$  where the shock occurs and then the loss dramatically increases in the high speed simulation due to the component of shock loss. Perdichizzi (1990) also demonstrated that the net secondary loss downstream of the trailing edge continually increases up to an exit Mach number of 0.9.

Although the shock does have a detrimental effect on the flow through the passage, it has been shown that there is only a small effect associated with the endwall secondary flows upstream of the trailing edge. This can be explained by considering the non-dimensionalized pitchwise pressure drop through the passage shown in Figure 18. This non-dimensionalization gives a measure of the pitchwise acceleration across the vane surfaces. The pressure drop is larger for most of the passage due to the compressibility of the flow. This difference in pressure drop would create much strong secondary flows for the high speed case; however, the pitchwise gradients are balanced by the increased streamwise pressure gradient along the vane surfaces resulting in nearly equal secondary flows and losses. This argument does not hold outside the confinements of the vane passage as confirmed by the analyses of Perdichizzi (1990) and Koiro and Lakshminarayana (1996).

Figures 11-18 have demonstrated that the flowfield associated with the baseline case has been accurately modeled with the low-speed, scaled-up simulations (both experimentally and computationally) up to the shock position. The results from the low speed parametric study are also applicable to engine conditions. Total pressure loss cannot be

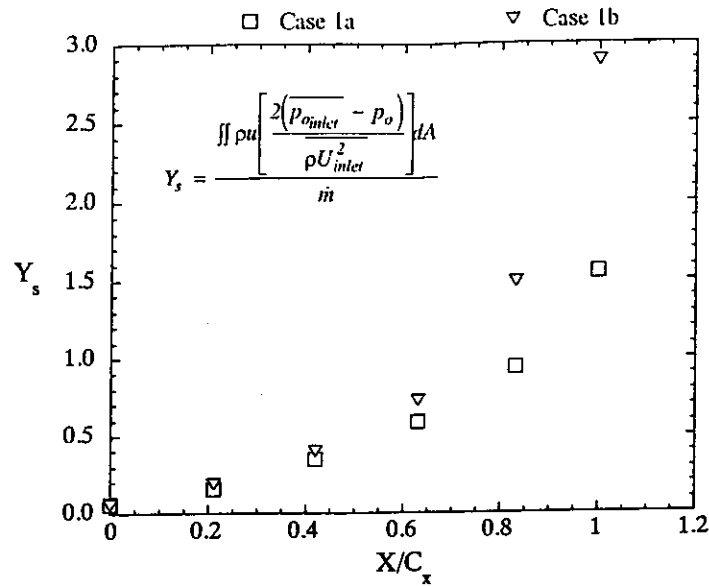


Fig. 17: Total pressure loss,  $Y_s$ , for baseline case at low Mach number conditions, Case 1a, and high Mach number conditions, Case 1b.

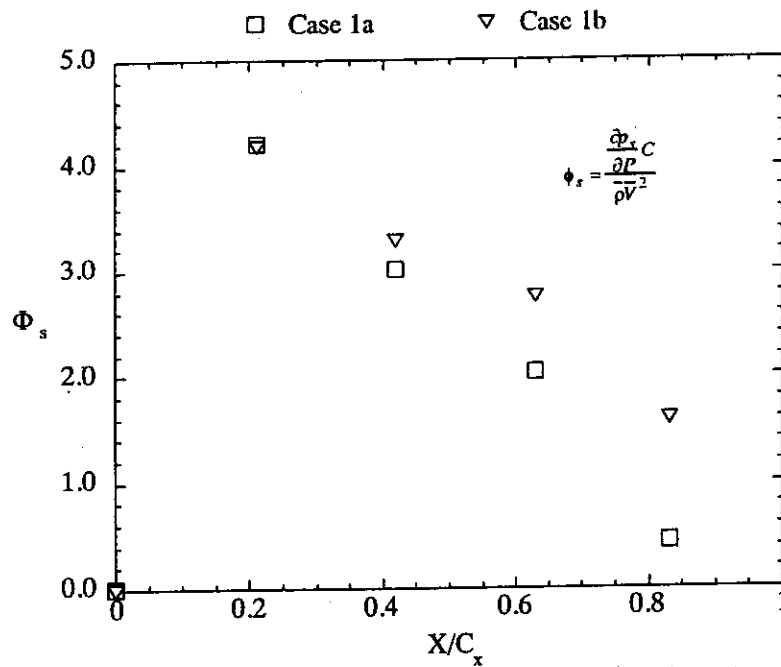


Fig. 18: Nondimensional pitchwise pressure drop,  $\Phi_s$ , for baseline case at low Mach number conditions, Case 1a, and high Mach number conditions, Case 1b.

accurately predicted by the low speed simulations. No effect of the fore-loaded vs. aft-loaded conditions of low speed and high speed pressure distributions was seen on the development of

secondary flows inside the passage. The effect of the shock was seen outside of the endwall region as flow moved toward the suction surface at the midspan.



## Conclusions

Prior to studying the effects of inlet conditions on secondary flows, CFD predictions from a baseline case were successfully benchmarked against flowfield measurements at low Mach number conditions using a scaled-up vane. The effects of spanwise inlet profiles on the development of secondary flows were determined from a study consisting of four cases. Results from the baseline case yielded a flow model similar to that of Langston (1980).

Three cases with various combinations of inlet velocity and temperature profiles were compared with the baseline case to determine the effect of spanwise temperature gradients. An analysis in the leading edge region was used to verify that the spanwise total pressure gradient is the driving factor for determining the magnitude of secondary flows in the passage. The secondary flows that develop at the leading edge are a factor of the inlet total pressure gradients and give a measure of the streamwise vorticity occurring downstream in the passage. No vortex structures form in the absence of a spanwise total pressure gradient; however, some streamwise vorticity occurs near the endwall as a boundary layer develops and a cross-flow velocity component is formed. Temperature contours showed that the secondary flow pattern distorts the temperature profiles for each case corresponding to the magnitude and direction of the secondary flows. The results demonstrate the need to consider realistic combustor exit profiles in stator design.

The flow patterns for the high and low speed conditions were very similar up to the shock location for the high Mach number case. This verified the region of applicability for the low speed wind tunnel experiments. Detailed comparisons of the secondary flows at low and high Mach number conditions showed that the increase in pitchwise pressure gradient at engine conditions is balanced by the increased acceleration along the pressure and suction surfaces. Downstream of the trailing edge the relative magnitude to streamwise and secondary velocities reduces the flow deviation for the high Mach number condition. The total pressure loss for

the high speed cases was much greater due to the loss associated with the shock occurring on the suction surface. The total pressure gradient is the key to determining the secondary flows for high and low Mach numbers.

## Acknowledgements

The authors gratefully acknowledge the support of Bill Kvasnak and Fred Soechting at United Technologies-Pratt & Whitney on this project.

## References

- Boyle, R.J. and Giel, P.W. (1997), "Prediction of Nonuniform Inlet Temperature Effects on Vane and Rotor Heat Transfer," ASME Paper 97-GT-133.
- Butler, T.L., Sharma, O.P., Joslyn, H.D., and Dring, R.P. (1989), "Redistribution of an Inlet Temperature Distortion in an Axial Flow Turbine Stage," *AIAA J of Propulsion and Power*, Vol. 5, No. 1, pp. 64-71.
- Crawford, M.E. (1986), "Simulation Codes for Calculation of Heat Transfer to Convectively-Cooled Turbine Blades," 130 pp., a set of 4 lectures in Convective Heat Transfer and Film Cooling in Turbomachinery, T. Arts, ed., Lecture Series 1986-06, von Karman Institute for Fluid Dynamics, Rhode-Saint-Genese, Belgium.
- Crocker, S. C., Nickolaus, D., and Smith, C. E., (1998), "CFD Modeling of a Gas Turbine Combustor from Compressor Exit to Turbine Inlet", ASME Paper 98-GT-184.
- Dorney, D.J., Davis, R.L., Edwards, D.E. and Madavan, N.K. (1992), "Unsteady Analysis of Hot Streak Migration in a Turbine Stage," *AIAA J of Propulsion and Power*, Vol. 8, No. 2, pp. 520-529.
- Fluent Inc., Fluent User's Guide (1998), Version 4.2. (Fluent Inc.: New Hampshire)

- Graziani, R. A., Blair, M. F., Taylor, J. R. and Mayle, R. E. (1980), "An Experimental Study of Endwall and Airfoil Surface Heat Transfer in a Large Scale Turbine Blade Cascade," *ASME J of Engineering for Power*, Vol. 102, pp. 257-267.
- Gregory-Smith, D. G., Graves, C.P., and Walsh, J. A. (1988), "Growth of Secondary Losses and Vorticity in an Axial Turbine Cascade," *ASME J of Turbomachinery*, Vol. 110, pp. 1-8.
- Halls, B. A. (1970), "Nozzle Guide Vane Cooling," AGARD, CP No. 73, Paper 25.
- Hawthorne, W. R. (1951), "Secondary Circulation in Fluid Flow," *Proc. Roy. Soc. A*, Vol. 206, pp. 374-387.
- Hermanson, K.S. and Thole, K.A. (2000), "Effect of Inlet Conditions on Endwall Secondary Flows," *AIAA J of Propulsion and Power*, Vol. 16, No. 2, pp. 286-296.
- Johnson, P.D. (1996), Personal communication.
- Kang, M., Kohli, A., and Thole, K.A. (1998), "Heat Transfer and Flowfield Measurements in the Leading Edge Region of a Stator Vane Endwall," *ASME J of Turbomachinery*, Vol. 121, No. 3, pp. 558-568.
- Kang, M. and Thole, K.A. (1998), "Flowfield Measurements in the Endwall Region of a Stator Vane", ASME Paper 98-GT-188.
- Koiro, M. and Lakshminarayana, B. (1996), "Simulation and Validation of Mach Number Effects on Secondary Flow in a Transonic Turbine Using a Multigrid, k- $\epsilon$  Solver," ASME paper 96-GT-544.
- Kvasnak, W. (1997), Personal communication.
- Lakshminarayana, B. (1975), "Effects of Inlet Temperature Gradients on Turbomachinery Performance," *ASME J of Engineering for Power*, Vol. 97, pp. 64-74.
- Langston, L. S. (1980), "Crossflows in a Turbine Cascade Passage," *ASME J of Engineering for Power*, Vol. 102, pp. 866 - 874.
- Launder, B.E. and Spalding D.B. (1974), "The Numerical Computation of Turbulent Flows," *Computer Methods in Applied Mechanics and Engineering*, 3:269-289.
- Loos, H. G., (1956), "Compressibility Effects on Secondary Flow," *J. Aeronautical Sciences*, Vol. 23, pp. 76-80.
- Moffat, R.J., (1988), "Describing the Uncertainties in Experimental Results," *Experimental Thermal and Fluid Science*, Vol. 1, pp. 3-17.
- Pantankar, S.V. (1980), *Numerical Heat Transfer and Fluid Flow*, Hemisphere, Washington, D.C.
- Perdichizzi, A., (1990), "Mach Number Effects on Secondary Flow Development Downstream of a Turbine Cascade," *ASME J. of Turbomachinery*, Vol. 112, pp. 643-651.
- Rai, M.M, and Dring, R.P., (1990), "Navier-Stokes Analyses of the Redistribution of Inlet Temperature Distortions in a Turbine," *AIAA J. of Propulsion and Power*, Vol. 6, pp. 276-282.
- Sharma, O. P. and Butler, T. L. (1987), "Predictions of Endwall Losses and Secondary Flows in Axial Flow Turbine Cascades," *ASME J of Turbomachinery*, Vol. 109, pp. 229-236.
- Sieverding C. M. and Wilputte, P., (1981), "Influence of Mach Number and End Wall Cooling on Secondary Flows in a Straight Nozzle Cascade," *ASME J. of Engineering for Power*, Vol. 103, pp. 257-263.
- Stabe, R.G, Whitney, W.J., and Moffitt, T.P. (1984), "Performance of a High-Work Low-Aspect Ratio Turbine Tested with a Realistic Inlet Radial Temperature Profile," AIAA Paper 84-1161.
- Suo, M. (1985), "Turbine Cooling" in *Aerothermodynamics of Aircraft Engine Components*, G.C. Oates editor, American Institute of Aeronautics and Astronautics, Inc. publisher.
- Yakhot V., Orszag S., Thangman, S., Gatski, T.B., and Speziale, C.G. (1992), "Development of Turbulence Models for Shear Flows by a Double Expansion Technique," *Phys. Fluids A* 4 (7), pp. 1510-1520.